Tellus (1996), 48A, 553–571
Printed in UK – all rights reserved

TELLUS
ISSN 0280–6495

Changes in predictability associated with the PNA pattern

HAI LIN* and JACQUES DEROME, *Department of Atmospheric and Oceanic Sciences and Centre for Climate and Global Change Research, McGill University, 805 Sherbrooke Street West, Montréal, Québec H3A 2K6*

(Manuscript received 11 August 1995; in final form 12 March 1996)

ABSTRACT

Numerical experiments are performed to determine whether the predictability of a model atmosphere is influenced by the presence of the Pacific/North American (PNA) pattern. The predictions are made with a T21 3-level quasi-geostrophic model. The relationship between the forecast errors and the "interannual" variation of the PNA anomaly is investigated. Comparison of the error growth for the forecasts made during the positive and negative PNA phases indicates that little difference in the error growth can be realized before about one week. After that period the forecast skill over the North Pacific, the North American and the North Atlantic regions is higher during the positive PNA phase than that during the negative PNA phase. A global signal of this relationship is also observed. The physical mechanism for the difference of error growth is discussed. For the forecasts made during the positive PNA phase, the pattern of systematic error has a negative PNA structure, while for the forecasts made during the negative PNA, the systematic error shows a positive PNA distribution. An explanation is given for the nature of the systematic error. This result implies that by selecting a set of particular anomalous observed cases, a bias is necessarily introduced into the model forecasts verified for these periods.

1. Introduction

As pointed out by Lorenz (1963, 1969), there is a limit to the predictability of the atmosphere due to the growth of errors which results from the imperfect knowledge of the initial conditions, even if the governing equations are deterministic and perfectly known. Charney et al. (1966) concluded, on the basis of three existing general circulation models, that the limit of predictability is about two weeks for synoptic-scale or larger-scale flows.

Efforts have been made to reduce the impact of the initial errors on predictions. As suggested by Charney (1960), the limit of predictability may be extended by taking a spatial or temporal average of the predictions. This can be explained by the fact that the large-scale field does not change rapidly, and that the initial errors grow less rapidly for the lower frequency components (Lorenz, 1969). Epstein (1969) proposed the use of a stochastic-dynamic forecast to predict the state of the atmosphere and to measure the uncertainty in the forecast. Leith (1974) discussed the Monte Carlo approach which takes an average of several perturbed forecasts. Recently a two-member ensemble method was used to improve the quality of the forecasts (Toth and Kalnay, 1992; Houtekamer and Derome, 1994).

The initial errors grow in different ways from case to case and considerable variability in predictive skill has been noted by some early predictability studies. Mansfield (1986) discussed the extended range forecast skill of the UK Meteorological Office 5-layer model over 18 winter-time cases with initial conditions from December 1974 to December 1981. He noted that although on average the anomaly correlation for

* Corresponding author
Email: hlin@zephyr.meteo.mcgill.ca

these forecasts fell to zero by about 19 days, some forecasts had exceptional skill. Miyakoda et al. (1986) reported on the analysis of eight extended range forecasts with the GFDL model. Their 30-day-mean scores also showed great interannual variability.

It would be interesting to study how the growth of initial errors depends on the type of weather regime or regime transition that is predicted or observed. From the assessment of the extended range forecasts of Mansfield (1986) and Miyakoda et al. (1986), and from the medium range forecasts at the ECMWF, Palmer (1988) noted that the skill of numerical forecasts is strongly influenced by the amplitude of the PNA (Pacific/North American) mode of low-frequency variability (Wallace and Gutler, 1981). He further argued on the basis of a barotropic stability analysis that the growth of the initial errors should be stronger in a basic flow having a negative PNA index (positive height anomaly over Aleutian Islands) than in a basic flow with a positive PNA index. Chen (1990) investigated the interannual variability of predictive skill of NMC medium-range forecasts, and found that over the Pacific/North America sector the skill was higher during El Niño winters than during non-El Niño winters.

Difficulties exist if one wants to use the forecast data from operational models to study the relationships between forecast errors and the low-frequency modes of variability. Although medium range forecasts have been run operationally in NWP centres for several years, a homogeneous dataset covering many years is still not available. As the forecast systems are modified from time to time, it is difficult to separate the effect of low-frequency variability from that of model improvements on the forecast skill.

In the present study, we use a simple 3-level quasi-geostrophic model to perform a large number of forecast experiments. We compare the predictability and the systematic error pattern in the positive and negative phases of the PNA pattern, one of the most important low-frequency modes in the atmosphere. We also investigate the mechanisms for the error growth by analyzing the development of the transients with time scales of 10–90 days.

In Section 2, we present the climatological features of the long-time control run, and the simulated structure of the interannual variability of the extratropical circulation. Section 3 contains the experimental design for the forecasts. In Section 4 we give the averaged behaviour of the forecast experiments. The comparison of the error growth in the positive and negative PNA phases is made and possible reasons of their differences are discussed in Section 5. Finally, our results are discussed in Section 6.

2. Control run and the "interannual" variability

The model used in this study is the spectral, three-level quasi-geostrophic model developed by F. Molteni at the European Centre for Medium-Range Weather Forecasts (ECMWF). It has a global domain and pressure as the vertical coordinate. The horizontal resolution of the model is triangular 21 (T21). For a detail description of the model, readers are referred to Marshall and Molteni (1993). The model is forced with a time-independent forcing field which enables the model to have a reasonable climatology. The forcing field was calculated from the daily (12 GMT) analyses of the ECMWF for a period of 9 winter seasons from 1980/81 to 1988/89, where the winter is defined as December, January and February.

With the external forcing obtained from the winter observations, a "perpetual winter" integration is performed. After an initial spin-up period of 360 days, model output data are saved once per day for 31485 days. This long-time integration is called the control run. These 31485 days are divided into 300 independent winters of 90 days by omitting the 15 days between consecutive 90 day periods. Also the long-time integration will serve as a reference atmospheric state which is also called the "truth". It is against this reference state that all predictability experiments discussed in the later sections will be compared. The model output in streamfunction is converted into geopotential height using the linear balance equation.

2.1. *The model climatology*

By computing the time-independent external forcing field with observations, the hope is that the long-term integration of the model will reproduce the observed wintertime mean flow and transients in a realistic way. It is important in our study that the model can reproduce a reasonably realistic climatology, especially the planetary-scale troughs over the east coasts of Asia and North America, which lead to localized regions of instability. Then low-frequency circulation patterns resembling those of the atmosphere to some extent may be expected.

Comparing the simulated and the observed mean 500 hPa streamfunction fields for the Northern Hemisphere, Marshall and Molteni (1993) demonstrated that the model is able to simulate the planetary-scale stationary waves in quite a realistic way. Our integration produced a similarly reasonable stationary wave pattern.

In order to extract the low-frequency eddies and the synoptic-scale transients, a Fourier time spectral filter is applied to each winter with consecutive 90 days. Transients with periods shorter than 2 days are removed. By definition here, the synoptic-scale transients have a frequency range corresponding to periods between 2 and 10 days, while the low-frequency eddies have periods from 10 to 90 days. The distributions of the standard deviation of the low-frequency transients for the model and the ECMWF analyses are presented in Figs. 1a, b, respectively. The ECMWF analyses are the same as those used to compute the model's forcing, i.e., daily (12 GMT) analyses for a period of 9 winter seasons from 1980/81 to 1988/89, where the winter is defined as December, January and February. The two maxima over the northeast Pacific and the north Atlantic are well reproduced. The distribution of the simulated high-frequency standard deviation is also in reasonably good agreement with the observations (not shown).

We conclude that the model has realistic stationary planetary waves and that the broad climatological characteristics of the transients are in general agreement with the observations. We consider that the differences between the model results and the observations are acceptable, since it is not our purpose to reproduce perfectly every aspects of the observed climatology.

2.2. *Simulated "seasonal" anomalies*

Our purpose is to study some aspects of atmospheric predictability in different circulation patterns. It will thus be important that the model be able to simulate the main features of important anomaly patterns that are observed in the atmosphere.

The PNA pattern describes one of the most significant teleconnections in ther atmosphere (Wallace and Gutzler, 1981). In this study, we will focus on the PNA pattern to investigate the dependence of the predictability on the presence or absence of this circulation pattern.

One way to describe the variability of the PNA pattern is to use the PNA index. The index is calculated for the "seasonal" mean flow (90-day average), and is defined following Wallace and Gutzler (1981) as

$$\begin{aligned}\text{PNA Index} = \frac{1}{4}[&z^*(20°\text{N}, 160°\text{W}) \\ &-z^*(45°\text{N}, 165°\text{W}) \\ &+z^*(55°\text{N}, 115°\text{W}) \\ &-z^*(30°\text{N}, 85°\text{W})], \qquad (1)\end{aligned}$$

where z^* represents a departure of a particular winter season (90 days) from the 300 winter mean 500 hPa height for that grid point, normalized by the local standard deviation of that departure. The positive (negative) PNA index is associated with negative (positive) height anomalies over the North Pacific and Florida and positive (negative) height anomalies over Hawaii and northwest Canada (see Fig. 2a).

In order to demonstrate the difference of the atmospheric states between the winters with positive and negative PNA indices, in the following we present the differences between them in the seasonal mean flow, the low-frequency variabilities and the synoptic-scale transients. Separate composites are made for the winters with extreme positive and negative PNA indices. The winters chosen for the composites are those with the PNA indices larger than $+\sigma$ and those smaller than $-\sigma$, where σ is the standard deviation ($\sigma = 0.68$) of the PNA index time series. We will refer to those winters with a PNA Index $>\sigma$ and a PNA Index $<-\sigma$ as those with positive and negative PNA anomalies, respectively. There are 43 winters with a positive PNA anomaly and 49 winters with a negative PNA anomaly according to this criterion. A student t-test method is used here to analyze the significance of the difference between the two groups.

Fig. 2 shows the difference maps resulting from subtracting the composite of the negative PNA phase from that of the positive phase for the

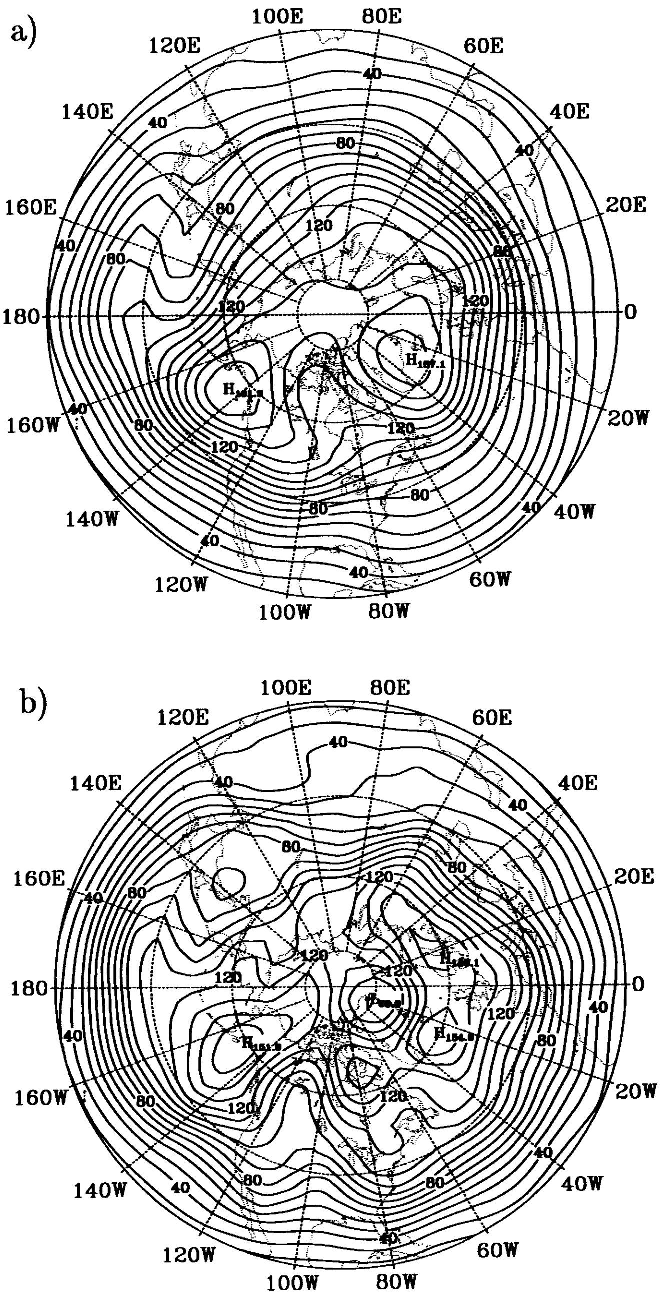

Fig. 1. Standard deviation of the low-frequency height field computed from (a) the QG model, and (b) the observations. Intervals are 8 m.

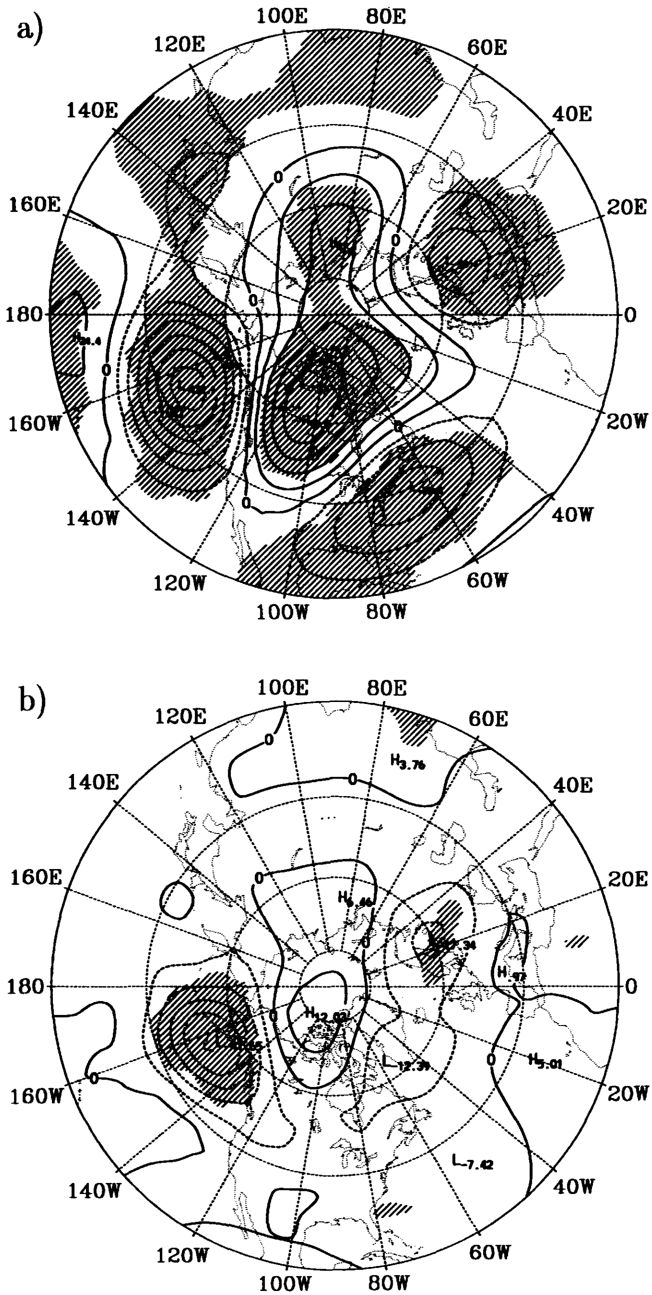

Fig. 2. Difference maps obtained by subtracting the statistics of model-produced 500 hPa geopotential heights of the negative PNA phases from that of the positive PNA phases for (a) the "seasonal" mean field; (b) the low-frequency standard deviation; (c) the high-frequency standard deviation. Contour intervals are 20 m for (a) and 8 m for (b) and (c). Areas with the student *t*-test significance levels greater than 99% are shaded.

c)

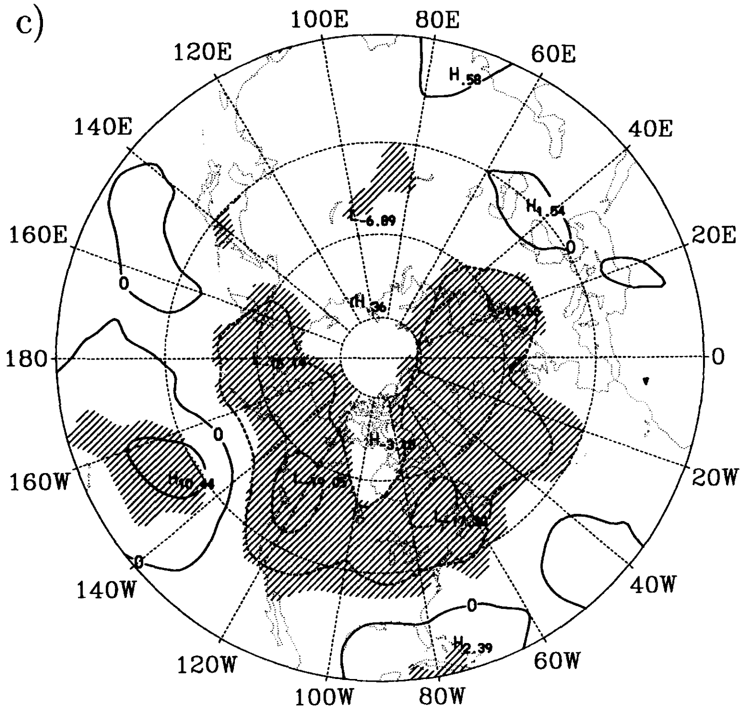

"seasonal" mean 500 hPa geopotential height, the low-frequency (10–90 days) height rms, and the high-frequency (2–10 days) rms. The shaded areas are those with t-test significance level exceeding 99%. The difference map of the composite 500 hPa geopotential height (Fig. 2a) clearly shows a PNA pattern, with high t-test significance level. During the periods with a positive PNA index (negative height anomaly over the Aleutian Islands), the low-frequency eddy activity is weaker in the North Pacific than during periods of a negative PNA index, and the high-frequency baroclinic waves are shifted to the east and south of their normal position in the Pacific. The difference map of the composite rms of the total transient (not shown) is similar to that of the low-frequency rms (Fig. 2b), indicating that the low-frequency eddies play a dominant role.

As is known, the observed PNA may be a combined result of internal dynamics and external forcing. The present study among others (e.g., Lau, 1981) provides evidence that PNA pattern can be generated without a varying external forcing. To give an idea of how strong the PNA variability in the model is with respect to the observed PNA pattern, a similar composite difference as Fig. 2a is made for the observed wintertime seasonal mean 500 hPa geopotential height using 24-year (1965–88) data from the U. S. National Meteorological Center (NMC), where winter is defined as 90 days starting from 1 December. A comparison of Fig. 2a with its observed counterpart (not shown) indicates that the structure of the observed composite anomaly is qualitatively rather well represented by the model, even over Europe and northern Asia. Over the North Pacific, however, the amplitude of the model anomaly is only 65% of the observed one, whereas over western Canada and the southeastern U.S. the model anomalies reach 92% and 165% of the observed ones.

3. The forecast experiments

We have seen that the model can produce a realistic climatology and "interannual" variabilities, including the PNA teleconnection pattern on the seasonal time scale. The modifications of the transients with different time scales during the positive and negative PNA phase resemble those in the observations (Lin, 1995). Thus this model provides a suitable tool to study some aspects of the relationship between the predictability and the PNA circulation anomaly.

A "perfect model" approach is used in this study. The perpetual winter control run discussed above will serve as a proxy for the atmospheric observations. Thus 300 independent "winters" are available for the forecast experiments.

Forecast experiments are performed for every winter. Fig. 3 shows schematically the design of the experiment for one winter. Starting from t_1, each experiment lasts 15 days. For each period of 90 days, t_1 = day 21 and t_1 = day 65 are chosen. From each t_1, two integrations are performed after adding different perturbation errors to the initial conditions. Thus there are 4 independent forecast experiments for every winter. We refer to the 2 integrations starting from t_1 = day 21 as E1 and E2, and the 2 experiments starting from t_1 = day 65 as E3 and E4. The number of total forecast experiments is 1200 for the 300 winters, of which there are 172 predictions for the positive PNA phase and 196 predictions for the negative PNA phase according to the criteria described in the last section.

To obtain the initial errors, the breeding method introduced by Toth and Kalnay (1993) is used. Instead of using a nonlinear approach as in Toth and Kalnay, we use the tangent linear model described by Houtekamer and Derome (1994). As

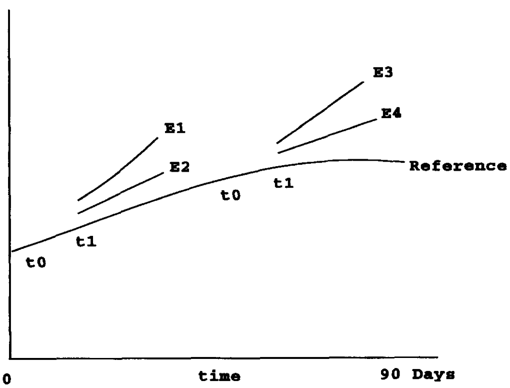

Fig. 3. Schematic representation of the forecast experiments.

discussed by Houtekamer and Derome, these two methods would yield similar bred modes. Starting from t_0, a tangent linear model is initialized with random numbers assigned to the amplitudes of the spherical harmonic coefficients and integrated to t_1 to obtain the "bred" perturbation. The tangent linear model, which was developed by Houtekamer and Barkmeijer, is the same model used to generate the reference orbit, but now linearized about the reference, time dependent atmospheric state. For each winter, t_0 is set to be day 1 for t_1 = day 21 and day 45 for t_1 = day 65, respectively. Thus to obtain the bred mode, the tangent linear model has been integrated for 20 days. The nature of the bred modes have been discussed by Houtekamer and Derome (1994). Due to the simple fact that the initial random perturbations will amplify most in directions that provide maximum growth, by the end of 20-day period the bred perturbations will be aligned in the directions of fastest sustainable growth in the model.

The "bred" perturbation streamfunction is scaled to have a globally and vertically integrated rms value equal to 10% of the model climatological rms value of the total transient part of the streamfunction. The latter was obtained from a previous 5-year integration of the model and found to be 2.5×10^{-3} in the units of $2\Omega a^2 = 0.59 \times 10^{10}$ m²/s, where Ω is the angular velocity of the earth and a the earth's radius. At t_1, the perturbation is added to the reference state to yield the initial condition for a perturbation experiment. If ψ_T represents the "true" value of the streamfunction, as given by the reference orbit in Fig. 3, and ψ_E is the analysis error which is simulated by the bred mode, the initial state for the forecast experiment is then given by

$$\psi_F(t=0) = \psi_T(t=0) + \psi_E\,. \qquad (2)$$

With two sets of different random numbers assigned to the amplitudes of the spherical harmonic coefficients at t_0, the tangent linear model is integrated to get the two initial errors. As for the control run, the forecast streamfunction is saved 1 × per day.

4. Unstratified errors

In order to give a general comparison of the forecasts and the "observations", we first present the error features averaged for the 1200 forecasts. Because a "perfect model" approach is used, a systematic modeling error averaged for the 1200 forecasts should not exist. A common way to measure the error growth is the error variance of the forecasts, which is defined as:

$$E = <(\psi_f - \psi_o)^2>, \tag{3}$$

where ψ_f is the forecast streamfunction and ψ_o is the corresponding "observed" streamfunction, the angle brackets indicating a global and vertical average.

Fig. 4 shows the forecast error variance averaged over the 1200 forecasts as a function of time. The vertical bars represent the standard deviation among the 1200 forecasts. The model forecasts show considerable variability in the forecast skill. The horizontal dashed line represents the climatological variance value of the transient part of the streamfunction. It can be seen from the figure that the forecast error variance, on average, reaches the climatological value at about 12.5 days.

To have an idea of the distribution of the forecast error, the rms of the 5-day mean 500 hPa geopotential height error is calculated. At a grid point at 500 hPa, the rms error is defined as:

$$E_{\mathrm{rms}} = \left(\frac{1}{N-1}\sum_{i=1}^{N}(\overline{Z_f} - \overline{Z_o})^2\right)^{1/2}, \tag{4}$$

where $\overline{Z_f}$ is a 5-day averaged forecast geopotential height at 500 hPa and $\overline{Z_o}$ is the corresponding

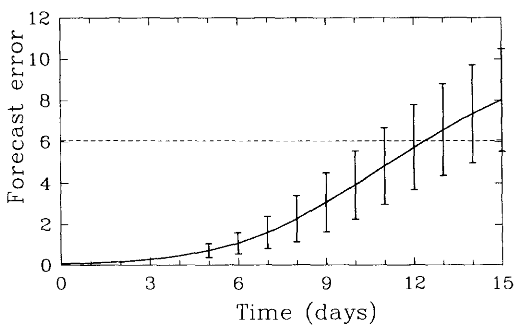

Fig. 4. The streamfunction forecast error variance in units of 10^{-6} averaged over 1200 forecasts as a function of the forecast length. The vertical bars represent the standard deviation among the experiments at that time. The horizontal dashed line is the climatological variance value of the transient part of streamfunction.

"observed" geopotential height, $N = 1200$ is the total number of experiments.

Fig. 5 shows the distribution of rms error of the 500 hPa geopotential height averaged over days 6 through 10. The maximum error occurs over the northeast Pacific and north Atlantic. The pattern of the rms error looks similar to the distribution of the low-frequency geopotential height standard deviation (Fig. 1a). The low-frequency variability is usually associated with slowly changing systems or persistent anomalies such as large storms that have entered the dissipating stage and become quasi-stationary, slowly moving upper air lows with closed height contours and blocking ridges, etc. In other words, the areas of large forecast errors are located in the same regions as blocking ridges and the slowly changing systems. The ability of numerical models to predict such low-frequency systems is in general very poor (Miyakoda et al., 1972).

5. Errors stratified by the phase of PNA

As can be seen from the standard deviation of the error variance among the 1200 forecasts in Fig. 4, the model forecasts show considerable variability in skill. We now turn to investigate the dependence of the forecast skill on the phase of the PNA pattern.

5.1. *Total error*

To show the difference in the error growth between the positive and the negative PNA phases, the forecast error variances are composited for the two conditions. As stated earlier, from the control run of 300 independent winters, 43 of them are identified as having a positive PNA phase and 49 as having a negative phase.

We have performed 4 forecast experiments (E1, E2, E3 and E4) for each winter. Composites of the forecast error variance are computed separately for E1, E2, E3 and E4 (each has 300 forecasts). Fig. 6 shows the forecast error variances in ψ as a function of lead time, which is again a globally and vertically averaged quantity as in Fig. 4. The solid lines represent the composites for the positive PNA phase, while the dashed lines represent the composites for the negative PNA phase. They represent the composites of the forecast error variance for E1, E2, E3 and E4. The

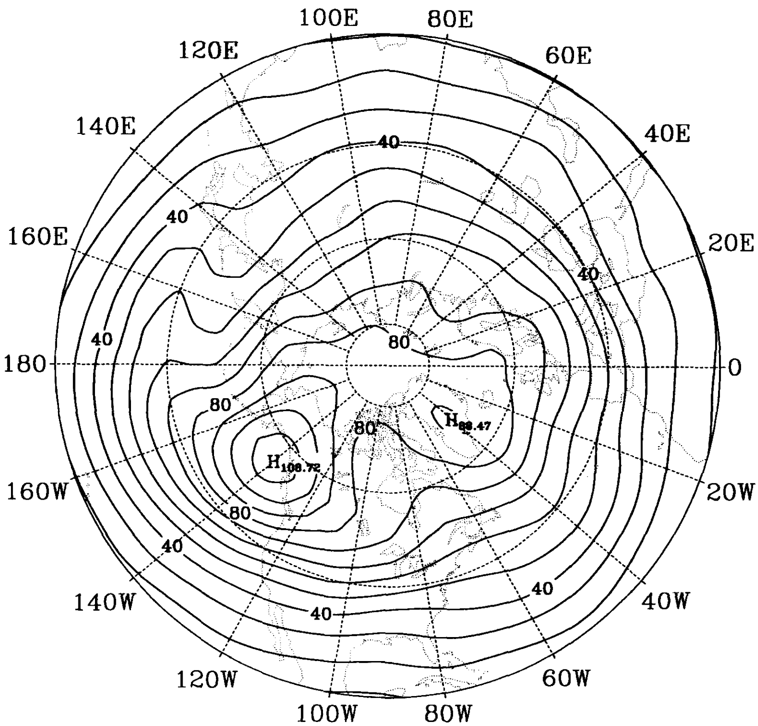

Fig. 5. Distribution of rms error of 500 hPa geopotential height of 5-day averages for days 6–10. Contour interval is 8 m.

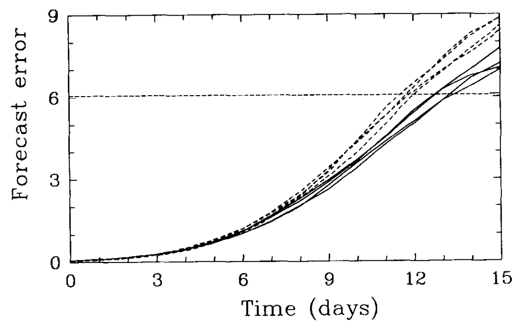

Fig. 6. The streamfunction forecast error variance in units of 10^{-6} as a function of forecast day for the positive PNA phase (solid lines) and the negative PNA phase (dashed lines). They represent the composites for E1, E2, E3 and E4.

purpose of presenting E1 ... E4 graphs is to assess the effect of sampling. we see that during the first 6 days the curves are almost identical. At about day 6 and the dashed and solid lines start to separate, and their difference develops as the lead time increases. This feature is true for all of E1, E2, E3 and E4. Thus even for a global average, the skill of the medium-range forecasts made during the positive PNA phase is higher than that made during the negative PNA phase.

To show the local features of the difference in the error growth between the positive PNA and negative PNA phases, Fig. 7 depicts the composite difference rms error of the 500 hPa geopotential height averaged over days 6–10 between the positive and negative PNA index winters. Negative values are found over most of the middle and high latitudes. The maximum difference is located along the latitude belt of 40°–60°N, with 2 negative centres of high significance levels located over the North Pacific and North America.

At later times the error keeps growing. Fig. 8 is obtained by subtracting the rms error over days 11–15 for the negative PNA phase from that for the positive PNA. From Fig. 8 it is seen that the rms error difference has been intensified from Fig. 7. A major negative centre is located over the

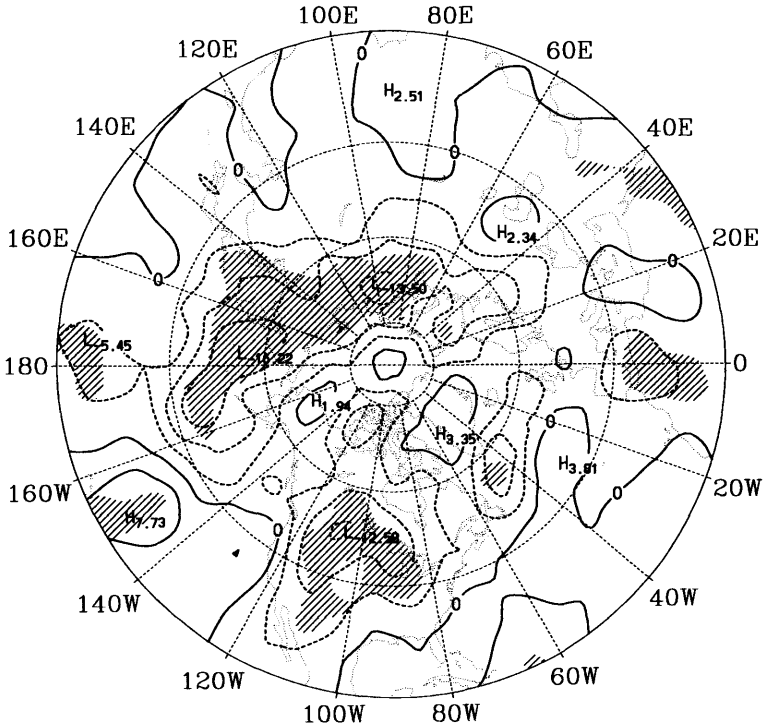

Fig. 7. Difference composite by subtracting rms error of 500 hPa geopotential height averaged over days 6–10 for negative PNA phase from that for positive PNA phase. The shaded areas represent regions with significance level exceeding 95%. Contour interval is 8 m.

North Pacific, and another one can be found over the North Atlantic. An area of positive values can be found south of 50°N off the west coast of North America, where the forecast error is larger for the predictions during the positive PNA phases than that during the negative PNA phases.

When the same rms error composites as in Fig. 7 and Fig. 8 are made for the forecast rms error averaged for days 1–5 (not shown), almost no difference can be found between the positive and the negative PNA phase. The PNA low-frequency variation indeed has little influence on the short range forecasts. This is consistent with Palmer and Tibaldi (1986) who found no correlation between the short range forecast skill over the PNA region and the quasi-stationary PNA-like mode of variability of the forecast flow.

We have seen that the error growth depends on the geographical locations. Comparisons are now made of the growths of the forecast error variances averaged in four different areas. Shown in Fig. 9, areas I and IV are located over the North Pacific and North Atlantic, respectively. Area II is over the eastern Pacific off the west coast of North America. Area III is over the North American continent. As can be seen, the 4 areas cover most of the midlatitude Pacific/North American region and its downstream North Atlantic region. Comparing with Fig. 8, it is seen that the negative centres in Fig. 8 over the North Pacific and North Atlantic are in areas I and IV, respectively. Area II includes the area of positive values observed off the west coast of North America. Composites of the forecast streamfunction error variances are computed separately for experiments E1, E2, E3 and E4 in the four areas. The forecast streamfunction error variances as a function of lead time in Area I, II, III and IV are shown in Figs. 10a, b, c and d, respectively. As in Fig. 6, the solid lines represent the composites for the positive PNA phase, while the dashed lines represent the composites for the negative PNA phase.

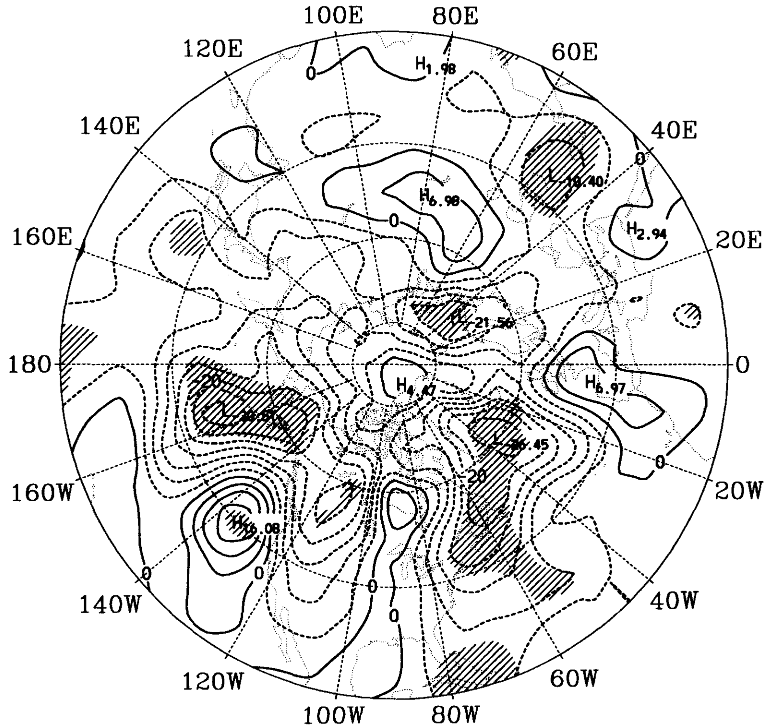

Fig. 8. As in Fig. 7, but averaged over days 11–15.

In Fig. 10b, the dashed and solid lines show no clear separation, indicating that in Area II the forecast skill bears no relation to the phase of the PNA pattern. The main features of Figs. 10a, c and d are similar to those of Fig. 6. Clearly, the forecasts after about one week during the negative PNA phase are worse than those during the positive PNA phase. In general, the four experiments E1, E2, E3 and E4 show similar characteristics. While the four solid lines in each figure are quite close to each other, the dashed lines show larger differences, indicating that the quality of medium-to-long range forecasts is less variable during the positive PNA phases than those during the negative PNA phases.

We conclude that the growth of initial errors after about a week is correlated with the PNA phase of the slowly-varying circulation. The forecast error grows faster during a negative PNA phase than during a positive phase. This relation is clear in the regions of the North Pacific, North America and the North Atlantic. Although some areas have less significance, or may behave differently, there is a signal of the relationship on the global scale.

The above result is consistent with that of Palmer (1988) who analyzed the ECMWF forecast data and found that the skill of the medium range forecasts (day 9) over the Pacific/North American region is strongly correlated with the signed amplitude of the PNA mode.

5.2. *Systematic error*

In this section, we compare the systematic error patterns in the 500 hPa height fields during the positive and negative PNA phases. It would be interesting to know the relationship between the systematic error and the phase of the PNA pattern, in which case the forecast error could be corrected if we know the amplitude and phase of the PNA pattern during which the prediction is made.

Figs. 11a and b show the systematic error patterns averaged for days 11–15, as obtained from 172 predictions in the positive PNA phase and 196 predictions in the negative PNA phase,

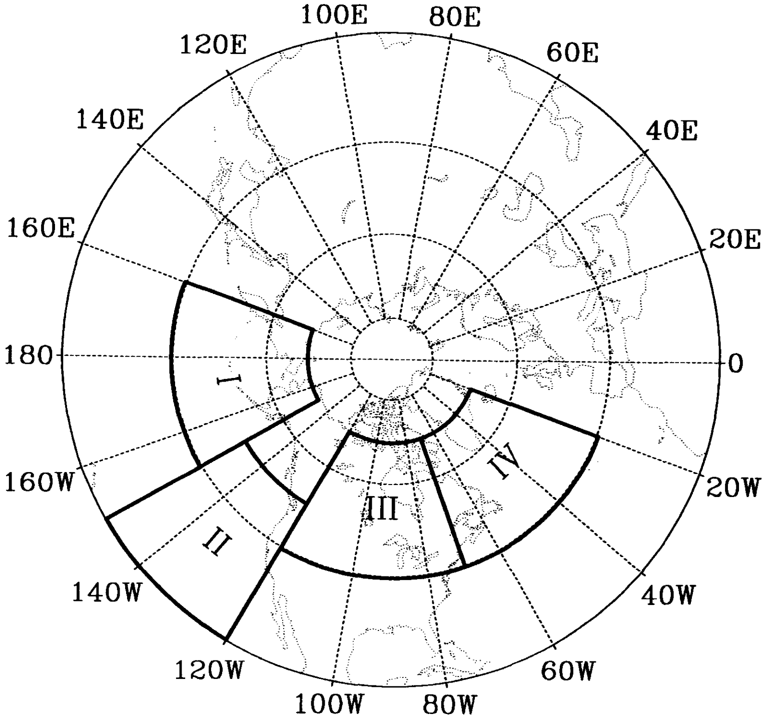

Fig. 9. Comparison areas. I: 40–70°N, 160°E–150°W; II: 20–50°N, 150°W–120°W; III: 40–70°N, 120°W–70°W; and IV: 40–70°N, 70°W–20°W.

respectively. We observe that the error patterns are opposite in sign to the PNA pattern of the reference state, i.e., when predictions are made during the positive (negative) PNA phase the error tends to be a negative (positive) PNA pattern. The difference map (not shown) shows a clear negative phase PNA pattern, with positive errors over the North Pacific and negative errors over the northwest part of North America. The systematic error patterns averaged for days 6–10 (not shown) reveal very similar features as in Fig. 11, except for weaker amplitudes.

Similar results have been reported by earlier studies from operational forecast data. Using the medium range forecast data set of the U.S. National Meteorological Center (NMC) for 7 years, O'Lenic and Livezey (1988) showed the dependence of the systematic error of the numerical forecasts on some of the low-frequency 700 hPa height patterns. They noted the tendency for the error patterns to be in opposite phase to the observed PNA. From a sample of the European Centre for Medium Range Weather Forecasts (ECMWF) operational 10-day forecast data, Molteni and Tibaldi (1990) also found that a regime-dependent component exists in the systematic error fields, with its pattern opposite to the anomaly of the observed flow regime.

From the present analysis of the large set of forecast experiments, and by the use of "perfect model" approach in which we consider the systematic error not to be influenced by the model's imperfection, we can confirm that there is a negative correlation between the systematic error and the slowly-varying PNA pattern. This error pattern depends only on the weather regime phase.

Molteni and Tibaldi (1990) explained the regime-related error in the framework of a stochastically-perturbed dynamical system. They used the Fokker–Planck equation to show that a reduction in the variance of stochastic perturbations causes a further increase of the frequency of the regime corresponding to the highest density maximum, and a decrease of the frequency of others.

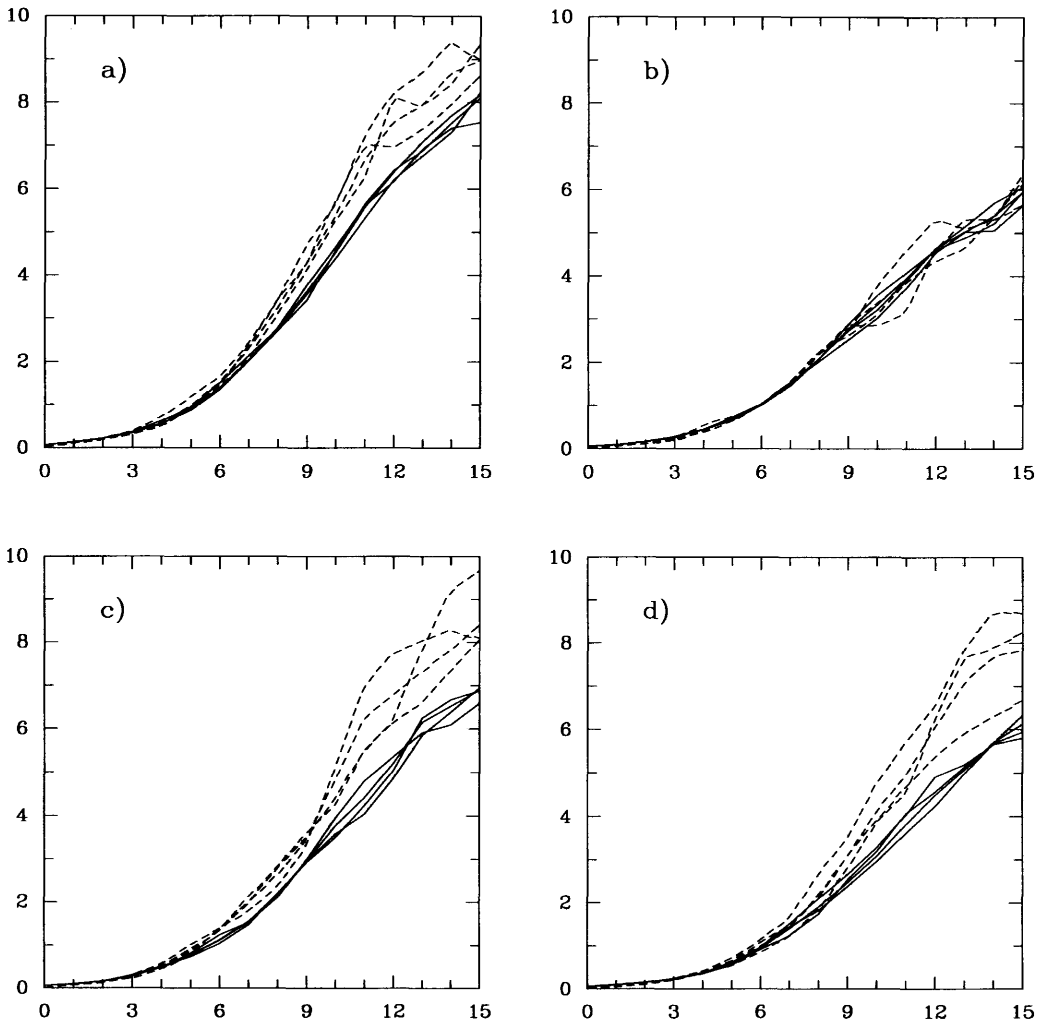

Fig. 10. The streamfunction forecast error variance in units of 10^{-6} as a function of forecast day for positive PNA phase (solid lines) and negative PNA phase (dashed lines). a), b), c) and d) are for areas I, II, III and IV, respectively. Composites of E1, E2, E3 and E4 are shown for each area.

Thus models in which the variance of the stochastic perturbations is reduced tend to relax the flow towards its most densely populated regime. In their study the reduction of the stochastic eddy variance was meant to simulate the fact that even state-of-the-art general circulation models can not represent all sources of variability.

In our study, because the model used for the forecasts is exactly the same as that used to obtain the "truth", there is no reduction in the variance of stochastic perturbations and a model deficiency cannot be blamed for the regime-related systematic error.

The model we used is a nonlinear system with a stationary external forcing. All the variabilities produced are caused by the internal processes. On the other hand, the external forcing is designed in such a way that the model can have a reasonable climatology. A set of integrations of the model for a sufficient long time should yield the same climatology no matter what initial conditions are used. In other words, the climatological behaviour of

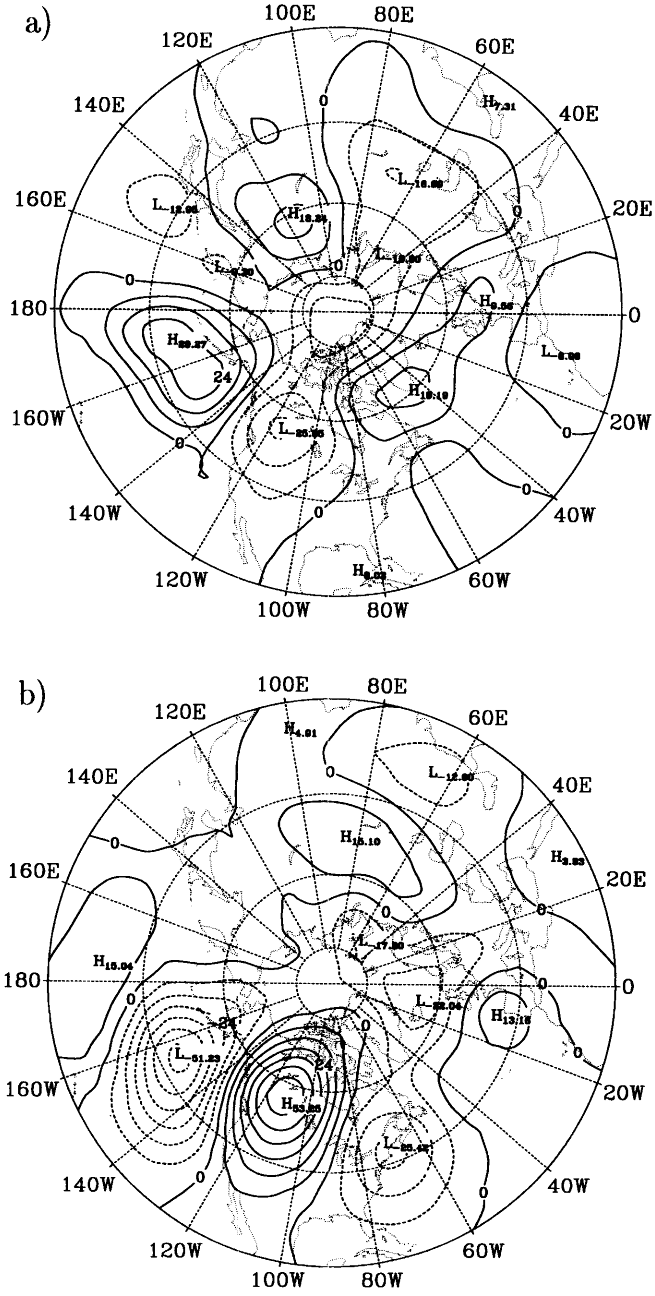

Fig. 11. Distribution of systematic error of 500 hPa geopotential height of 5-day average for days 11–15 for (a) positive PNA phases; (b) negative PNA phases.

the system will be independent of the initial conditions after some time, i.e., the details of initial conditions will be forgotten.

Keeping the above points in mind, let us discuss how the regime-related systematic error happens in our experiments. As forecast experiments are made during positive or negative PNA phases, initial conditions are selected when the atmosphere has a strong anomaly, i.e., it is in a less likely area of the phase space. Obviously, since these situations happen rarely (only 172 or 196 cases out of 1200 cases), several specific factors need to coincide in the initial conditions for these scenarios to realize. So if we change the initial condition, it is more likely that we will loose this special development (on which we based our selection criteria) than not. If each forecast is made for enough long time, the average state of the forecasts will be close to the climatology. Therefore, for the forecasts during the positive PNA phases, a systematic error (forecast-truth) with a negative PNA pattern is obtained. Similarly a systematic error with a positive PNA pattern is expected for those forecasts performed during the negative PNA phase, as obtained in this study. In short, the negative correlation between the forecast error and the flow pattern indicates that the forecasts tend to underestimate the amplitude of the slowly-varying teleconnection pattern.

From Figs. 11, it can also be seen that for the negative PNA, the systematic error is larger than for the positive PNA. Considering that at infinite lead time the systematic error would be zero, the model approaches its mean state more quickly from a negative PNA pattern than from a positive one, meaning that a negative PNA pattern is more unstable in this sense than a positive one. This is consistent with the difference in the total error presented in the previous subsection.

5.3. *Discussion*

Considering that the difference between the forecast errors of the positive and the negative PNA phases emerges after about 6 days, it is reasonable to believe that the development of the low-frequency eddies plays an important role. Comparing Fig. 8 with Fig. 2b, we see that the difference map of the error patterns between the positive PNA phase and the negative phase is rather similar to that of the corresponding low-frequency transient rms, suggesting that the weaker intraseasonal fluctuations during the positive PNA phase are related to the smaller rms errors. In the following we discuss the mechanisms behind the "interannual" variability of the low-frequency eddy activity. By understanding why the low-frequency eddy activity is weaker during a positive PNA phase than during a negative PNA phase, we can better understand why the forecast errors are weaker in one situation than in the other.

The output of the 300 winter control run is used here to do the analysis. As mentioned in Section 3, Fourier filters are used to obtain the low- and high-frequency components of the transients. Thus for a period of 90 days, the flow is decomposed into three parts: the time mean, the low-frequency part and the high-frequency part. The calculations are performed at 500 hPa. To explain the reduction of the low-frequency eddy activity during the positive PNA phases, we examine the interactions of the low-frequency fluctuations with the time mean flow and with the high-frequency eddies.

5.3.1. Barotropic energy exchange with the time mean flow. One kinetic energy source for the development of the low-frequency eddies is the barotropic energy exchange with the background mean flow. Following Simmons et al. (1983), the barotropic conversion of kinetic energy from the time mean to the low-frequency eddies, to a good approximation, can be written as:

$$C = \mathbf{E} \cdot \nabla \bar{u}, \tag{5}$$

where $\mathbf{E} = -(\overline{u_l^2 - v_l^2}, \overline{u_l v_l})$ is the extended Eliassen-Palm flux discussed in detail by Hoskins et al. (1983). u and v are the zonal and meridional velocity components, respectively. The overbar represents the time average and the subscript l refers to the low-pass filtered data.

To see the difference of the barotropic conversion of kinetic energy between the positive and the negative PNA period, comparison is made for the composites of C defined by (5) for these 2 cases. Fig. 12 shows the composite difference field of C between the positive and negative PNA winters. It is clear that the low-frequency eddies extract less kinetic energy in the central and north Pacific from the background mean flow when the PNA index is positive. A positive area in Fig. 12

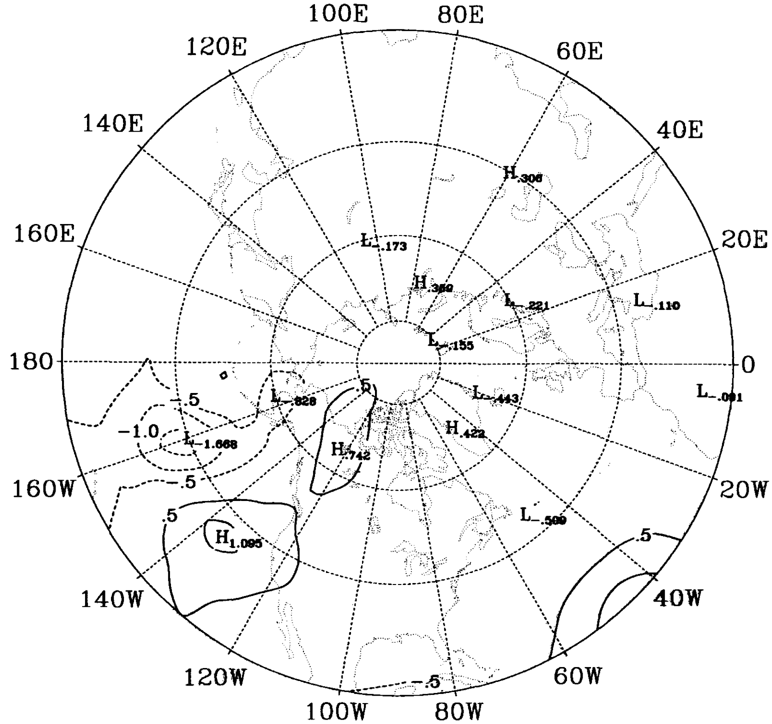

Fig. 12. Difference map obtained by subtracting the barotropic energy conversion in the negative PNA winters from that of the positive PNA winters. The contour interval is 0.5×10^{-4} W kg^{-1}.

in the eastern Pacific off the west coast of North America can be found, where the kinetic energy supply from the mean flow to the low-frequency eddies is stronger during the positive PNA phase. The distribution of the kinetic energy transfer difference over the Pacific areas is similar to Fig. 8. This suggests that the difference in the kinetic energy transfer from the mean flow contributes to the low-frequency eddy activity difference between the positive and negative PNA phases, and hence to the forecast error difference.

5.3.2. Barotropic high-frequency eddy forcing. Another important mechanism for the development of the low-frequency eddies is their interaction with the synoptic-scale transients. To get the distribution of the contribution by the interaction, we analyze the covariance between the low-frequency geopotential height and the height tendency caused by the vorticity flux convergence by the synoptic-scale eddies. This covariance can be expressed as:

$$\overline{z_l \frac{\partial z_l}{\partial t}} = -\frac{f}{g}\overline{z_l\, \nabla^{-2}\nabla\cdot(\mathbf{V}_h\zeta_h)_l}, \tag{6}$$

and the calculations are made at 500 hPa. As shown by Lau and Holopainen (1984), the high-frequency thermal forcing is very weak at this level, so that the high-frequency eddy vorticity forcing can approximately represent the net forcing at this level.

The composite difference distribution of the covariance between the low-frequency geopotential height and the height tendency caused by high-frequency eddy forcing is mapped in Fig. 13. Negative values dominate in the North Pacific and North Atlantic, indicating the high-frequency eddy forcing is reduced during the positive PNA winters. Over the eastern Pacific an area with positive values is located south of 45°N, implying that the location of the low-frequency forcing by the high-frequency transients is shifted southeast-

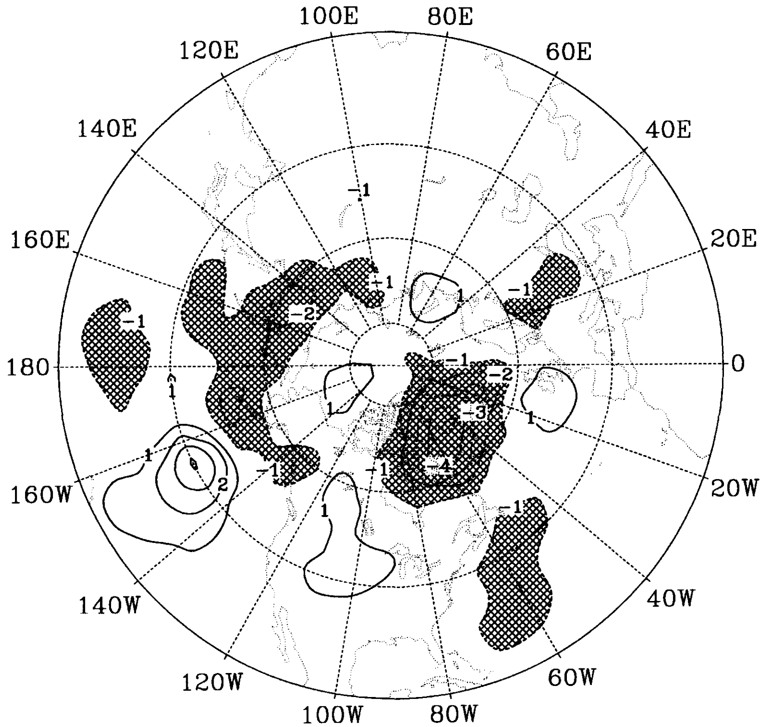

Fig. 13. Difference map obtained by subtracting the covariance between the low-frequency geopotential height and the synoptic-scale eddy forcing in the negative PNA winters from that of the positive PNA winters. The contour interval is 1×10^{-3} m^2/s.

ward during positive PNA periods. Referring to Fig. 8, the negative centres over the North Pacific and North Atlantic and the positive value area in the eastern Pacific have their similarities in Fig. 13.

We have seen that two mechanisms may be involved to explain the weakness of the low-frequency activity, and the slower growth of errors over the North Pacific, the North American and the North Atlantic areas in medium- to long-range predictions during the positive PNA phase. Firstly, less kinetic energy is supplied to the low-frequency eddies from the large-scale seasonal mean flow because of its modified structure. This mechanism seems mainly to contribute over the Pacific area. Secondly, the strong seasonal mean Aleutian low tends to keep the baroclinic synoptic-scale eddies moving along its southern side, causing only a weak interaction with the low-frequency eddies in the Northern Pacific, and thus less synoptic-scale eddy forcing. During a positive PNA phase, the above normal geopotential heights over North America and the lower than normal heights to the southeast cause a reduction in the baroclinicity over the east coast of North America and the North Atlantic (Fig. 2a). Thus less active synoptic-scale eddies are expected over the North Atlantic (Fig. 2c), and less synoptic-scale eddy forcing to the low-frequency flows. In the case of weak synoptic-scale eddy forcing, an initial perturbation in the low-frequency eddies would develop less fast and lead to smaller forecast errors.

Palmer (1988) investigated the barotropic instability problem for the positive and negative Pacific/North American (PNA) phases, and found that during the negative PNA phase the atmosphere is more unstable to low-frequency disturbances. Medium range forecast errors over the North Pacific would therefore seem more likely to develop during the negative PNA phase. This is consistent with our first mechanism discussed above in that the kinetic energy transfer from the seasonal mean flow to the low-frequency transients is stronger over the central and northern Pacific during the negative PNA phase than that during the positive PNA phase. The present study indicates that the interaction between the high- and low-frequency eddies is also important for the interannual variability of the low-frequency eddies and the error growth in the forecasts.

This study suggests that the medium range weather forecasts made during El Niño winters, when the circulation pattern tends to be in the positive phase of the PNA, should show smaller r.m.s. errors over the North Pacific and North American region than those made during non-El Niño winters. Whether this is indeed the case will have to be tested with statistics derived from state-of-the-art forecast models.

6. Summary and conclusions

In this study, we have used a 3-level Q-G model to conduct a large number of forecast experiments. The relationship between the forecast behaviour and the "interannual" variation of the PNA anomaly has been investigated. The main purpose was to identify cases that are more predictable than others.

The Q-G model was forced by a time-independent external forcing to produce a realistic climatology. A control run was performed for 300 winters. The "interannual" variability of the seasonal mean flow was investigated. We found that the model was able to produce significant "interannual" variability.

A perfect model approach was used where the perpetual winter control run served as a proxy for the atmospheric observations. Forecast experiments were made from the initial conditions by adding to the reference state some analysis errors, which were simulated by bred modes.

A comparison of the forecast error growth during the positive and negative PNA phases was made by composite analysis. Little difference of the error growth can be seen before about a week. Subsequently the error grows faster when the forecasts are made during the negative PNA phase. The forecast skill for the medium-and long-range predictions over the North Pacific, North American and the North Atlantic regions is higher during the positive PNA phase than that during the negative PNA phase. The physical mechanisms for the difference in the error growth were discussed. We found that the weaker intraseasonal fluctuations during the positive PNA phase are responsible for the smaller rms errors. The intraseasonal fluctuations develop by extracting kinetic energy from the seasonal mean flow and through the barotropic interaction with the high-frequency eddies. We have seen that during the positive PNA phase the low-frequency transients extract less kinetic energy from both sources.

We have also compared the average error patterns in the 500 hPa height fields during the positive and negative PNA phases. A negative correlation between the systematic error and the slowly-varying PNA pattern was observed. Based on the fact that all the variabilities in our model are caused by internal nonlinear processes and that the system has a single climatology, the regime-dependent systematic error was explained. For the medium range forecasts made during the positive (negative) PNA phase, the averaged atmospheric state should lie between the climatology and the initial state which has a positive (negative) PNA pattern. Thus the systematic error has a negative (positive) PNA pattern.

7. Acknowledgements

This research was supported by research grants from the Natural Sciences and Engineering Research Council and the Atmospheric Environment Service of Canada. We are indebted to Dr. Franco Molteni for his permission to use the three-level quasi-geostrophic model. We are grateful to Dr. Zoltan Toth whose comments helped to clarify parts of this paper.

REFERENCES

Charney, J. G. 1960. Numerical prediction and the general circulation. In: *Dynamics of climate* (ed. R. L. Pfeffer), Pergamon, 12–17.

Charney, J. G., Fleagle, R. G., Lally, V. E., Riehl, H. and Wark, D. Q. 1966. The feasibility of a global observation and analysis experiments. *Bull. Amer. Meteor. Soc.* **47**, 200–220.

Chen, W. Y. 1990. Interannual variability of skill of

NMC medium-range forecasts over the Pacific/North America sector. *Mon. Wea. Rev.* **118**, 179–188.

Epstein, E. S. 1969. Stochastic-dynamic prediction. *Tellus* **21**, 739–759.

Hoskins, B. J., James, I. N. and White, G. H. 1983. The shape, propagation and mean-flow interaction of large scale weather systems. *J. Atmos. Sci.* **40**, 1595–1612.

Houtekamer, P. L. and Derome, J. 1994. Prediction experiments with two-member ensembles. *Mon. Wea. Rev.* **122**, 2179–2191.

Lau, N.-C. 1981. A diagnostic study of recurrent meteorological anomalies appearing in a 15-year simulation with a GFDL general circulation model. *Mon. Wea. Rev.* **109**, 2287–2311.

Lau, N.-C. and Holopainen, E. O. 1984. Transient eddy forcing of the time-mean flow as identified by geopotential tendencies. *J. Atmos. Sci.* **41**, 313–328.

Leith, C. E. 1974. Theoretical skill of Monte Carlo forecasts. *Mon. Wea. Rev.* **102**, 409–418.

Lin, H. 1995. *On the interaction among the extratropical atmospheric transients of different frequencies.* Ph.D. thesis, Department of Atmospheric and Oceanic Sciences, McGill University, Montreal, Quebec, 147 pp. (available as McGill C^{2}GCR Report No. 95-2).

Lorenz, E. N. 1963. Deterministic nonperiodic flow. *J. Atmos. Sci.* **20**, 130–141.

Lorenz, E. N. 1969. The predictability of a flow which possesses many scales of motion. *Tellus* **21**, 289–307.

Mansfield, D. A. 1986. The skill of dynamical long-range forecasts, including the effect of sea surface temperature anomalies. *Q. J. R. Meteorol. Soc.* **112**, 1145–1176.

Marshall, J. and Molteni, F. 1993. Toward a dynamical understanding of planetary-scale flow regimes. *J. Atmos. Sci.* **50**, 1792–1818.

Miyakoda, K., Hembree, G. D., Strickler, R. F. and Shulman, I. 1972. Cumulative results of extended forecast experiments. 1: Model performance for winter cases. *Mon. Wea. Rev.* **100**, 836–854.

Miyakoda, K., Sirutis, J. and Ploshay, J. 1986. One month forecast experiments—without anomaly boundary forcing. *Mon. Wea. Rev.* **114**, 2363–2401.

Molteni, F. and Tibaldi, S. 1990. Regimes in the wintertime circulation over northern extratropics. II: Consequences for dynamical predictability. *Q. J. R. Meteor. Soc.* **116**, 1263–1288.

O'Lenic, E. A. and Livezey, R. E. 1988. Relationships between initial circulation anomalies and forecast errors. In: *Predictability in the medium and extended range.* ECMWF Workshop Proceedings, 311–339.

Palmer, T. N. 1988. Medium and extended range predictability and stability of the Pacific/North American mode. *Q. J. R. Meteorol. Soc.* **114**, 691–713.

Palmer, T. N. and Tibaldi, S. 1986. *Forecast skill and predictability.* ECMWF Technical Memorandum No. 127.

Simmons, A. J., Wallace, J. M. and Branstator, G. W. 1983. Barotropic wave propagation and instability, and atmospheric teleconnection patterns. *J. Atmos. Sci.* **40**, 1363–1392.

Toth, Z. and Kalnay, E. 1992. Growing modes of the atmosphere obtained by "breeding" and their application to ensemble forecasting. In: *Proceedings 2nd International Conference on Modelling of global climate change and variability.* Hamburg, 84–87.

Toth, Z. and Kalnay, E. 1993. Ensemble forecasting at NMC. The generation of perturbations. *Bull. Amer. Meteor. Soc.* **74**, 2317–2330.

Wallace, J. M. and Gutzler, D. S. 1981. Teleconnections in the geopotential height field during the Northern Hemisphere winter. *Mon. Wea. Rev.* **109**, 784–812.